Advanced Powder Materials 4 (2025) 100318

Contents lists available at ScienceDirect

Advanced Powder Materials

journal homepage: www.keaipublishing.com/en/journals/advanced-powder-materials

Second-phase composite engineering endows Gd_3TaO_7-based ceramic with broadband infrared radiation

Enyu Xie [a,b,c], Shuqi Wang [a,b,c,*], Guoliang Chen [d,e,**], Yongchun Zou [a,b,c], Jianghong Zhang [f], Yaming Wang [a,b,c,***], Qingyuan Zhao [a,b,c], Zijian Peng [a,b,c], Junteng Yao [a,b,c], Jiahu Ouyang [a,b,c], Dechang Jia [a,b,c], Yu Zhou [a,b,c], Valentina L. Stolyarova [g]

[a] State Key Laboratory of Precision Welding & Joining of Materials and Structures, Harbin Institute of Technology, Harbin 150001, China
[b] Institute for Advanced Ceramics, Harbin Institute of Technology, Harbin 150001, China
[c] Key Laboratory of Advanced Structure-Function Integrated Materials and Green Manufacturing Technology, Harbin Institute of Technology, Harbin 150001, China
[d] Key Laboratory of Aerospace Thermophysics, Harbin Institute of Technology, Harbin 150001, China
[e] Ministry of Industry and Information Technology, Harbin Institute of Technology, Harbin 150001, China
[f] School of Materials Science and Engineering, Nanyang Technological University, 639798, Singapore
[g] Saint Petersburg State University, Universitetskaya Nab.7/9, 199034, Saint Petersburg, Russia

ARTICLE INFO

Keywords:
Tthermal radiation
Thermal conductivity
Thermal stability
Toughness
Tantalate-based-ceramics

ABSTRACT

High-temperature infrared (IR) radiation materials with broadband high emissivity, low thermal conductivity, and high fracture toughness are urgently needed for radiative heat management. Here, we report a Gd_3TaO_7/$GdFeO_3$ composite ceramic that integrates a broadband (0.78–14 μm) high emissivity (close to 0.9), low thermal conductivity (1.62 W m^{-1} K^{-1}), and fracture toughness (2.3 MPa $m^{1/2}$, close to YSZ). Through the introduction of second-phase $GdFeO_3$, many lattice distortions, multimode vibrations, and additional oxygen vacancies (O_v) contribute to an increase in the broad-band emissivity of the composite ceramics (especially in the 2.5–6 μm band, nearly 5 times greater than that of Gd_3TaO_7). This high IR emissivity significantly suppresses the elevated photonic thermal conductivity at high temperatures, resulting in ultralow thermal conductivity. Moreover, the stable atomic arrangement within the two phases contributed to the impressive high-temperature stability (1773 K, 200 h). The improved fracture toughness is attributed primarily to the presence of the second phase promoting crack tip deflection, bridging and branching, which prevent crack expansion. All the advantages render this second-phase composite strategy fully competitive in the development of a new generation of superhigh-temperature radiative heat management materials.

1. Introduction

Radiant heat management regulates energy transfer and conversion between systems via two methods (heat conduction and heat radiation) [1]. This technology provides crucial significance for energy conversion, energy-saving applications, and thermal insulation protection, which are of great strategic importance in aerospace [2], nuclear power engineering, energy [3] and chemical industries [4]. Reportedly, as the ambient temperature increases, the heat radiation transfer percentage in radiant heat management systems increases, especially at high temperatures (>1,073 K), almost approaching the share of thermal conduction [5]. According to the Stefan–Boltzmann law [6], in radiant heat management, the thermal radiation capacity is closely related to the infrared emissivity of the engineered thermal surface. However, it is not sufficient to merely concentrate on the photothermal conversion efficiency of the material at the membrane layer surface and ignore the heat conduction process of the heat flow inside the membrane layer for the application of heat management materials at high temperatures. Therefore, thermal management by controlling thermal radiation and thermal conduction, coupling high emissivity and low thermal conductivity, can play an effective role in

* Corresponding author. State Key Laboratory of Precision Welding & Joining of Materials and Structures, Harbin Institute of Technology, Harbin 150001, China.
** Corresponding author. Key Laboratory of Aerospace Thermophysics, Harbin Institute of Technology, Harbin 150001, China.
*** Corresponding author. School of Materials Science and Engineering Harbin Institute of Technology, Harbin 150001, China.
E-mail addresses: wang-shuqi@hit.edu.cn (S. Wang), chenguoliang@hit.edu.cn (G. Chen), wangyaming@hit.edu.cn (Y. Wang).
Peer review under the responsibility of Central South University.

https://doi.org/10.1016/j.apmate.2025.100318
Received 27 March 2025; Received in revised form 24 June 2025; Accepted 24 June 2025
Available online 4 July 2025

thermal protection at high temperatures, which has broad application prospects. For example, in a photovoltaic power generation system [7], it is necessary to maximize the conversion efficiency of thermal photons while minimizing the energy waste from thermal conduction. In high-temperature, energy-efficient industrial furnace systems [8], refractory walls with high emissivity and low thermal conductivity can significantly improve energy efficiency and fulfill energy-saving requirements. In aerospace flight systems [9], thermal protective coatings for hot-end components (e.g., space vehicle surfaces and engine blades) are desired to mitigate extreme high-temperature damage from heat fluxes via radiative heat dissipation and low thermal conductivity. Thus, in the aforementioned radiant heat management applications, especially in the thermal protection coating field, how to satisfy the maximum IR radiant heat dissipation (high emissivity) as much as possible while suppressing the residual heat transfer to the substrate surface (low thermal conductivity) is the core issue. Researchers have usually endeavored to address these issues by designing multilayer structures [10], surface microstructures [11], etc. Nevertheless, these strategies involve non-negligible challenges such as macroscopic large-size interfacial connections, thermal mismatch, weak mechanical strength, and insufficient thermal stability, which limit the safety and reliability of their application in harsh environments. Therefore, the development of a thermally protective material with high emissivity, low thermal conductivity, high-temperature stability, and adequate mechanical properties remains a major challenge.

To increase the emissivity over a wide spectral range over a wide temperature range (300–1,600 K), it is common to consider reducing the difficulty of increasing the electronic energy level and increasing the lattice vibration in the material design [12]. The electron energy level enhancement efficiency and lattice vibration strength affect emission/absorption in the visible/near-infrared (0.3–2 μm) and mid-infrared (2–14 μm) bands, respectively [13]. For example, by doping transition group metal ions or rare earth ions within the main lattice of existing materials, the introduction of impurity energy levels reduces the lattice bandgap, simultaneously induces lattice distortions, and improves the lattice vibration, which results in an increase in the broadband spectral emissivity [14]. However, this strategy inevitably greatly affects the corresponding thermophysical properties of the substrate material due to the alteration of its main lattice structure, which is an obvious weakness of the ion doping strategy. In addition, this ion doping strategy may lead to a decrease in the thermal stability of the material at high temperatures [15], and the strong immiscibility of ion doping between different crystal structures is a difficult challenge that cannot be ignored [16]. Hence, the introduction of high-absorption second-phase particles into the matrix phase is considered a new design strategy. Currently, ceramic systems such as $Gd_2Zr_2O_7$/Pt, $Gd_2Zr_2O_7$/$GdMnO_3$, $Sm_2Zr_2O_7$/-$NiCr_2O_4$, etc., have been synthesized and prepared by scholars and exhibit considerably high emissivities [17–19]. Finally, a major challenge in the application of ceramic materials is the trade-off between strength and toughness. Despite these great achievements, several scientific issues remain to be resolved, mainly focusing on both performance and mechanism, which can be subdivided into the following: I. difficulty in balancing broad-spectrum high emissivity, low thermal conductivity, and strong toughness; II. poor explanation of the second-phase particles enhancing the composite ceramic emissivity mechanism; III. unknown high-temperature thermal stability of high-emissivity composite ceramics. Thus, it is essential to obtain new TBC materials with high emissivities, low thermal conductivities, high toughnesses, and high-temperature thermal stabilities, as well as to further investigate the high-emissivity mechanism for the development of thermally protected coatings for radiative heat dissipation. Recently, weberite-type Gd_3TaO_7 has been considered a potential new-generation thermal barrier coating material due to its lower thermal conductivity (1.6–1.95 W m^{-1} K^{-1}) [20] and higher phase stability (above 1673 K) in ultrahigh-temperature service environments [21]; this is attributed to the higher relative ionicity and lower covalency of RE-O bonding, leading to stronger harmonic vibrations in the Gd_3TaO_7 lattice and its softer phonon modes and correspondingly lower acoustic velocities, resulting in a lower phonon thermal conductivity [22]. However, the increasing photonic thermal conductivity at high temperatures makes it difficult for the total thermal conductivity to reach the phonon thermal conductivity. The wider forbidden band and single vibrational mode result in a low broad-band infrared emissivity (<0.5), and the higher ionic bonding energy enables it to exhibit a relatively low fracture toughness (1.7 MPa $m^{1/2}$) [20]. Therefore, further investigations are needed to thoroughly explore the potential of the use of Gd_3TaO_7 in high-temperature thermal management materials (especially thermal barrier coating materials).

In this work, we propose the incorporation of diffusely distributed transition group oxide $GdFeO_3$ particles within the Gd_3TaO_7 base phase to significantly modify the thermal radiative and mechanical properties of TBC materials while maintaining their thermophysical properties and chemical stability at high temperatures. The results demonstrate the strong infrared emissivity (~0.9) of the $0.9Gd_3TaO_7/0.1GdFeO_3$ composite ceramics in the 0.78–14 μm band due to the small polariton effect caused by the variable valence behavior of Fe^{3+}/Fe^{2+} inside the $GdFeO_3$, the increasing oxygen vacancy concentration inside the Gd_3TaO_7/$GdFeO_3$, and the lattice vibrational absorption from the lattice distortion effect. Moreover, GTFO maintains a low thermal conductivity (1.62 W m^{-1} K^{-1}), benefiting from its high absorption properties, with a radiative thermal conductivity of only 0.02 W m^{-1} K^{-1}, and the upward warping of its high-temperature thermal conductivity curve is suppressed. In addition, the GTFO composite ceramics showed outstanding toughness (2.3 MPa $m^{1/2}$) and excellent thermal stability at 1773 K for 200 h. Compared with other TBC materials, GTFO has unrivaled comprehensive thermal, optical, and mechanical properties, indicating its potential for thermal protection in extreme environments and providing a solid theoretical foundation for the development of high-temperature infrared-radiating TBC materials.

2. Result and discussion

2.1. Synthesis and characterizations

We designed a brand-new composite tantalate ceramic material with a spherical second phase diffusely distributed arrangement, with the aim of simultaneously achieving the following properties: (1) high absorptivity in the near- and mid-infrared wavelength bands; (2) low thermal conductivity from room temperature up to 1473 K and inhibiting the high-temperature warping of the thermal conductivity curves; (3) excellent mechanical properties; (4) high-temperature (1,773 K) thermal stability for long-time service. Therefore, the calcite-type transition metal oxide $GdFeO_3$ was chosen as the second phase. In contrast to Gd_3TaO_7, which has an orthorhombic weberite structure, $GdFeO_3$ has a narrow bandgap, while it is easy to increase the carrier concentration and transition probability, resulting in a high light absorption/emission ability. Moreover, due to the introduction of the second phase, a predictable large number of oxygen vacancies and multimode vibrations are generated during the material synthesis process, which contributes to the tailoring of thermophysical and infrared radiation properties. Compared with the single-phase specimen (Gd_3TaO_7), $0.9Gd_3TaO_7/0.1GdFeO_3$ and $0.8Gd_3TaO_7/0.2GdFeO_3$ both exhibit excellent high emissivity in the infrared wavelength band (Fig. S1). When the molar percentage of $GdFeO_3$ was increased to 20%, the addition of the second phase would severely affect the thermophysical properties of the composites, resulting in a significant increase in thermal conductivity (Fig. S2), which is probably related to the high thermal conductivity property of $GdFeO_3$ itself. Therefore, the molar percentage of Gd_3TaO_7 to $GdFeO_3$ in the composites was optimized to 9:1 and marked with GTFO (Gd_3TaO_7 ceramics marked with GTO).

The GTFO ceramic with expected broad-spectrum high emissivity was synthesized by the solid-state reaction method (Fig. S3). The

microstructure of GTO ceramics sintered at different temperatures (1773 K, 1823 K, 1873 K, and 1923 K) were investigated, as shown in Figs. S4a, b, c, d. It was determined that the sintering temperature of GTO is supposed to be 1923 K, as well as based on the previous experimental experience, the GTFO ceramic was identified as sintered at 1823 K, and its grain size and relative porosity (1.28%) were similar to that of single-phase Gd_3TaO_7 ceramics sintered at 1923 K.

The XRD pattern of the GTO and GTFO samples in Fig. S5 shows a typical weberite features, in which a series of distinct diffraction peaks can be observed, where the crystal structure consists of TaO_6 octahedra, GdO_7 and GdO_8 polyhedral. And the diffraction peak of the $GdFeO_3$ (121) plane can be observed in the range of 32°–35°, corresponding to PDF#97-001-6644, whose local magnification is shown on the right side of Fig. S5. In addition, probably due to a minor diffusion of iron ions within $GdFeO_3$ into the main lattice, the (022) diffraction peak of GTFO is slightly shifted to a higher angle, which indicates lattice contraction. On this basis, the crystal structure of the GTFO sample was comprehensively analyzed using the Rietveld refinement method, which shows high crystallinity (Fig. 1a). And the primary cell parameter of GFTO (603.20 $Å^3$) is less than that of GTO (603.99 $Å^3$) (Table S1), which verifies the conclusion of lattice shrinkage deduced from the (022) peak displacement [23]. Fourier transform infrared spectroscopy (FT-IR, Fig. 1b) shows significant absorption peaks of GTFO around 480 cm^{-1} and 590 cm^{-1}, attributed to the deformation vibration of O–Fe–O and the stretching vibration of Fe–O, respectively. And the absorption bands around 2000 cm^{-1} are associated with adsorbed water molecules.

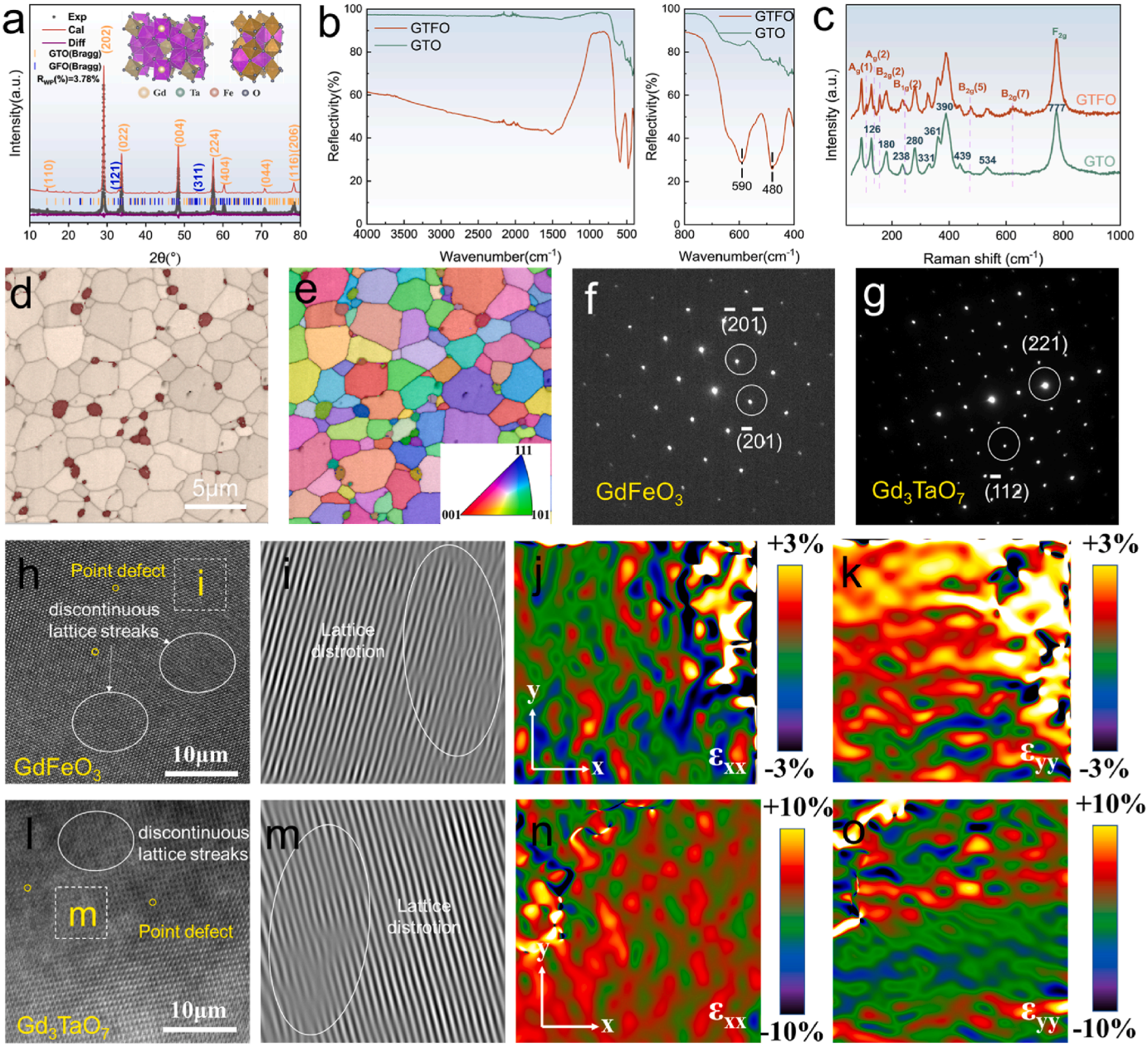

Fig. 1. (a) XRD Rietveld refinements of GTFO sample; (b) Fourier Transform Infrared (FT-IR) spectra of GTFO and GTO samples; (c) Raman spectra of GTFO and GTO samples; (d) EBSD phase map of the GTFO sample; (e) Corresponding EBSD inverse pole Fig. (IPF) map of the main phase of GTFO sample; (f) Selected Area Electron Diffraction (SAED) pattern of $GdFeO_3$; (g) Selected Area Electron Diffraction (SAED) pattern of Gd_3TaO_7; (h) HRTEM image of $GdFeO_3$ region; (i) Atomic lattice image of yellow-cubic region in (h); (j,k) Corresponding strain fields ε_{xx} and ε_{yy} were obtained by the GPA method based on (h); (l) HRTEM image of Gd_3TaO_7 region; (m) Atomic lattice image of yellow-cubic region in (l); (n,o) Corresponding strain fields ε_{xx} and ε_{yy} were obtained by the GPA method based on (l).

Fig. 1c compares the Raman spectra of the as-prepared Gd_3TaO_7 ceramics before and after $GdFeO_3$ compositing. The results indicate that there are 10 different vibrational peaks observed in the GTO sample, in which the Raman mode F_{2g} near 777 cm^{-1} belongs to the co-linear Ta–O–Ta bond in the TaO_6 octahedron, and this vibrational peak is one of the most remarkable features of the weberite phase. In contrast, besides the presence of the characteristic peaks of Gd_3TaO_7 in the Raman pattern of GTFO, there are six characteristic peaks belonging to $GdFeO_3$, where A_g (2) and B_{2g} (7) are the two most characteristic vibrational peaks. As known, the optical properties of material are greatly related to the stretching vibration of its internal bonding, and the appearance of the characteristic peaks from $GdFeO_3$ within the GTFO Raman spectra indicate a lateral enhancement to its optical properties. Especially in the infrared band after 2.5 μm, the emissivity of GTFO sample is significantly improved compared to that of GTO samples, as described in detail later. In addition, the thermal conductivity of GTFO can also be varied by the effect of internal lattice stretching vibrations [24].

In Fig.s S6a, b, it can be seen that both materials have more than 95% densification, excellent microstructure homogeneity without obvious defects, and macroscopic colors of off-white and black, respectively. Via BSE analysis, Fig. S6c demonstrates a magnified photograph of the $GdFeO_3$ phase in the GTFO sample, which is spherical in shape with the characteristic layer structure of $GdFeO_3$ inside. Moreover, the grain orientation and distribution of the two phases in the GTFO sample were shown with the support of EBSD analyses (Fig. 1d, e, and Fig. S7). The corresponding EBSD phase images confirm the orthorhombic structure of the Gd_3TaO_7 main phase (gray contrast), which has a diffuse distribution of near-spherical grains ($GdFeO_3$) of red contrast at its grain boundaries. Remarkably, the Inverse Polar Fig. (IPF) of Fig. 1e shows that the Gd_3TaO_7 main-phase grains are isometric grains with random crystallographic orientation. In addition, the grain sizes of GTO and GTFO, as well as the content of $GdFeO_3$ in GTFO, were obtained statistically by analyzing the above images. And the grain sizes of Gd_3TaO_7 in GTO and GTFO ranged from 3 to 5 μm, the size of $GdFeO_3$ in GTFO ranged from 1 to 1.5 μm, while the content of $GdFeO_3$ was about 8.9%, which is comparable to the design. The KAM (Kernel Average Misorientation) image (Fig. S7) is frequently used as an indirect indication of defects, dislocations, etc. within the material microstructure [25]. In particular, the color of the second phase and its surrounding main phase region exhibits a warmer hue compared to the other main phase regions, which implies that there is a large orientation difference inside the grains of this region, probably representing the high density of dislocations and crystalline defects therein, from which optical, thermal, and mechanical properties potentially benefited.

Additionally, the crystal structure of the two phases in GTFO was further revealed at the nanoscale with the assistance of TEM. From the bright-field images (Fig. S8a), high-angle annular dark-field (HAADF, Fig. S8b), and energy-dispersive X-ray spectra (STEM-EDS, Fig. S8b, I–V) of the selected regions, the interfaces of the two phases, Gd_3TaO_7 and $GdFeO_3$, are well defined, and the distributions of the four elements (Gd, Ta, Fe, and O) in the two phases are expected, indicating the coexistence within the two phases. The EDS line scan (Fig. S8c) corresponding to Fig. S8a also confirms the mentioned viewpoint. Further, SAED images (Fig. 1f and g) demonstrate the crystallization of $GdFeO_3$ and Gd_3TaO_7 in perovskite and weberite structures, respectively, which are in agreement with the previous crystal structure analysis. The magnified high-resolution TEM (HRTEM) images (Fig. 1h–l) and corresponding FFT images (Fig. 1i–m) reveal numerous structural defects including discontinuous lattice streaks, dislocations, point defects, etc., existing in the $GdFeO_3$ phase and its surrounding main-phase region. Meanwhile, the lattice strains are calculated with the support of the Geometric Phase Analysis (GPA) method (Fig. 1j, k, n, o), which further validate the "structure-rich defects" characteristic of the GTFO samples [26], thus contributing to their high infrared radiation properties, low thermal conductivity, and high ductility coupling.

2.2. IR radiation performance and thermal stability

For evaluating the optical properties of the GTO and GTFO samples as well as to investigate the thermal radiation mechanism, the infrared reflectance of the samples was measured, as shown in Fig. 2a. The GTFO sample exhibits an ultra-low reflectivity, which can be as low as 6% at 500 nm; on the contrary, that of the GTO sample is higher than 70% at 500 nm and even reaches 99% (1800 nm). It is noteworthy that the reflectivity of both samples shows a general upward trend with increasing wavelength, probably related to the weakened light absorption of Gd ions, and the absorption peak of the GTFO sample at 1000 nm might be attributed to the d-d leaps of iron ions. Obviously, the addition of $GdFeO_3$ significantly suppressed the reflectivity surge phenomenon of Gd_3TaO_7 at 1500 nm and 1800 nm, where the low optical absorption characteristics of GTO were remarkably improved.

Considering the organizational homogeneity of GTFO, with the support of Equivalent Medium Theory (EMT), the optical properties of each region can be regarded as consistent from a macroscopic point of view. Furthermore, the layer model and Kubelka-Monk theory were applied to simplify the photon transport process. The well-known Kubelka-Munk function F (R_∞) is listed below [27]:

$$\frac{(1-R_\infty)^2}{2R_\infty}=\frac{K}{S} \tag{1}$$

where R_∞ is the reflectivity of a very thick sample, K is the absorption coefficient, and S is the scattering coefficient.

The scattering coefficient, S, is related to R_∞ as follows [27]:

$$S=\frac{1}{h}\frac{R_\infty}{(1-R_\infty)} \tag{2}$$

where, h is the sample thickness.

Fig. 2b demonstrates the absorption coefficients of GTO and GTFO in relation to the wavelength, where GTFO exhibits absorption coefficients much higher than those of GTO in the whole wavelength band (400–2,000 nm) up to nearly 5×10 m^{-1}. Moreover, in order to quantitatively evaluate the optical absorption properties of $GdFeO_3$ in GTFO, the absorption factors (Q_{abs}) of $GdFeO_3$ grains in the Gd_3TaO_7 matrix are introduced and obtained from the following equation [18].

$$\alpha_{compos}=Q_{abs}\frac{3V_f}{2d} \tag{3}$$

where α_{compos} is the absorption coefficient of GTFO, V_f is the volume fraction of $GdFeO_3$ in Gd_3TaO_7 matrix, and d is the $GdFeO_3$ grain size.

Based on the microstructure picture of the GTFO sample in Fig. 1f, it can be assumed that the $GdFeO_3$ particles are diffusely distributed in a spherical form within the Gd_3TaO_7 matrix and have a diameter of 1.5 μm. In addition, the volume fraction V_f of $GdFeO_3$ particles is about 6.22% for the XRD Rietveld refinement data of Fig. 1a. As a result, the absorption factors (Q_{abs}) of $GdFeO_3$, as shown in Fig. 2b, is up to 0.7 (500 nm). Notably, the enhancement of the light absorption performance of $GdFeO_3$ particles for the Gd_3TaO_7 matrix as well could be reflected in the near-infrared band (NIR, 0.78–2.5 μm) transmittance spectra, as shown in Fig. S9. The GTFO samples exhibit extremely low transmittance (close to 0) in the NIR band, while the GTO samples reach up to an incredible 80%. Laterally, the transmission of NIR light to the GTFO sample is severely hindered by the strong absorption of NIR light by the $GdFeO_3$ particles, which contributes to the thermal protection performance of this material system.

Furthermore, with the aim of gaining insight into the effect of $GdFeO_3$ composite modification on the infrared radiative properties of Gd_3TaO_7 in broader wavelength bands, the spectral emissivity of GTFO and GTO as well as the irradiance relative to the blackbody have been investigated. Fig. 2c shows the IR emissivity spectra of both samples in the 2.5–14 μm band at room temperature. It is noteworthy that the IR emissivity of the GTO sample at 2.5–6 μm presents a trend of increasing

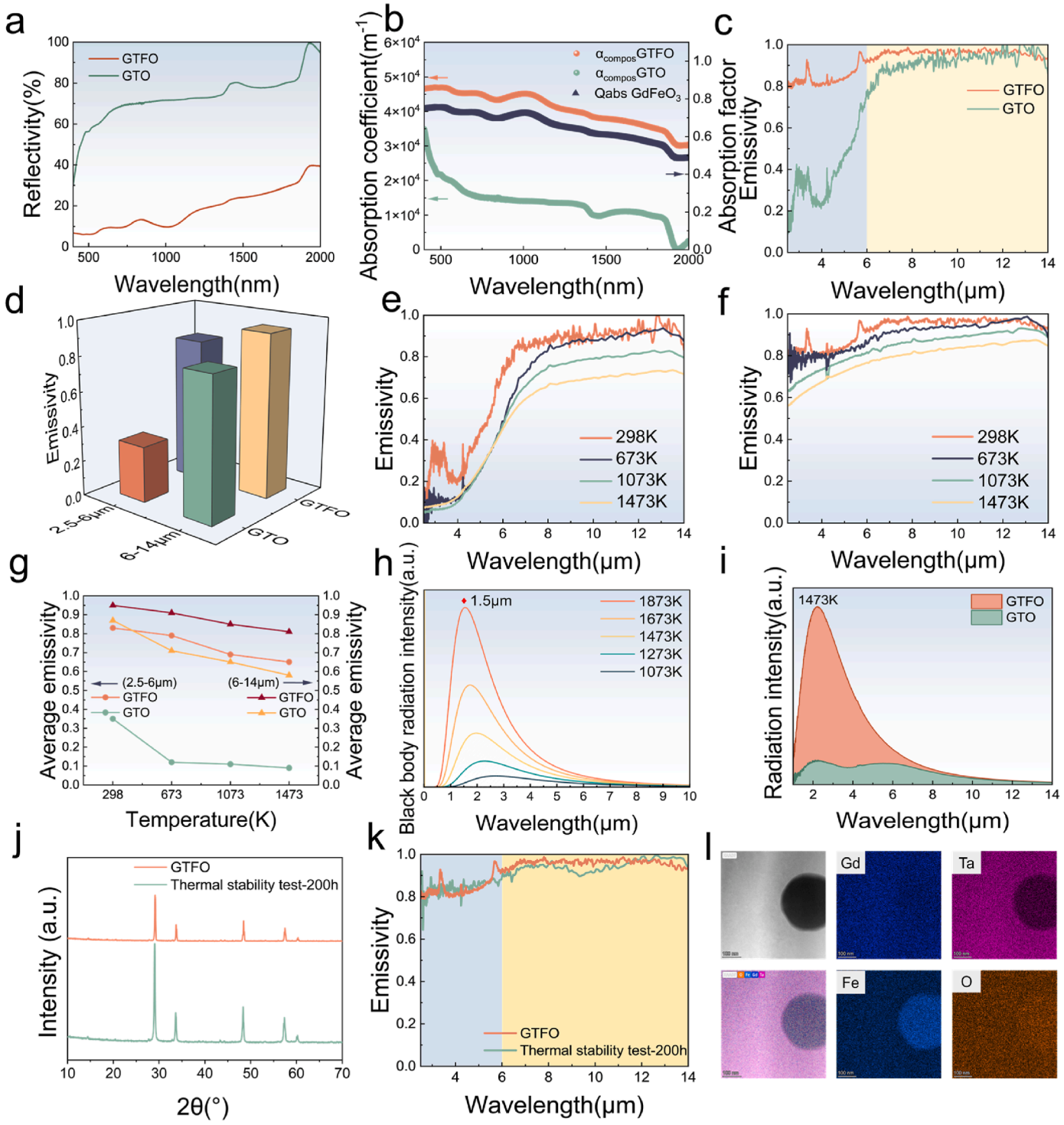

Fig. 2. (a) Reflectivity spectra of GTFO and GTO samples at room temperature; (b) Absorption coefficient spectra of GTFO and GTO samples; (c) Emissivity spectra from 2.5 to 14 μm of GTFO and GTO samples at room temperature; (d) Average emissivity spectra of (c); (e) Emissivity spectra from 2.5 to 14 μm of GTO sample at different temperature; (f) Emissivity spectra from 2.5 to 14 μm of GTFO sample at different temperature; (g) Average emissivity spectra of (e–f); (h) Emission spectra of regions associated with blackbody radiation at different temperatures; (i) Irradiance of GTFO and GTO at 1473 K; (j) XRD patterns of GTFO sample after thermal stability test at 1773 K for 200 h in air; (k). Emissivity spectra of GTFO sample after thermal stability test at 1773 K for 200 h in air; (l) Dark-field scanning transmission electron microscopy (STEM) image combined with energy dispersive X-ray spectroscopy (STEM-EDS) of GTFO sample after thermal stability test at 1773 K for 200 h in air.

and then decreasing, and the value of the emissivity is comparatively less, with the emissivity at 2.5 μm below 0.1, which in the much low category, while the IR incidence of the GTFO sample at 2.5–6 μm exhibits a steadily increasing trend, and the emissivity at 2.5 μm is above 0.8 (4 times higher than that of the GTO sample). When the IR band is > 6 μm, the GTFO sample still demonstrates a higher IR emissivity, approaching to 1. To quantitatively compare the IR emissivity of GTFO and GTO in the 2.5–14 μm band, we calculated their average emissivity

at 2.5–6 μm and 6–14 μm, respectively. The average emissivity of GTFO and GTO at 2.5–6 μm and 6–14 μm are 0.83, 0.28 and 0.97, 0.93, respectively, as shown in Fig. 2d. It can be affirmed that the improvement of the infrared radiation properties towards GTO is significant, and the composite modification method is extremely effective in enhancing the broad-spectrum infrared radiation properties of rare earth tantalates (the average emissivity of GTFO at 2.5–14 μm is close to 0.9).

Evaluating their high-temperature infrared radiation performance is key for high-temperature radiant heat protection. The application context of the GTFO composites in this work is, thus, needs to be edited. Hence, based on the wavelength range which can be detected by the detector at different temperatures, we characterized the high-temperature spectral emissivity of GTFO and GTO at 298 K, 673 K, 1073 K, and 1473 K, as shown in Fig. 2e and f. It can be observed that the emissivity of both samples decreases with increasing temperature in the 2.5–14 μm band. In combination with the average emissivity calculated in Fig. 2g, the negative effect of temperature on the high-temperature emissivity of GTO is more intuitive, i.e., the emissivity of GTO decreases more significantly when the same temperature is elevated. When the temperature is increased to 1473 K, the average emissivity of GTFO remains above 0.6 (0.62) in the 2.5–6 μm band, while that of GTO is as low as 0.14, with a fivefold difference. And the emissivity of GTFO and GTO are 0.76 and 0.61, respectively, in 6–14 μm. According to Planck's blackbody radiation law, the percentage of energy emitted at 1–14 μm versus 0–200 μm is about 97.6% when the temperature reaches the operating temperature of the current engine, 1400 K, and the maximum blackbody energy will move further into the near-infrared band as the temperature increases, as shown in Fig. 2h. Hence, we focus on the average emissivity in the infrared band (<14 μm) as an important reference for evaluating the infrared radiation performance of the material. And the radiative forcing curves (emissivity data * blackbody radiative forcing) of GTFO and GTO in different wavelengths at 1473 K were calculated as shown in Fig. 2i. In particular, the GTFO sample demonstrates much higher radiative intensity than that of GTO, displaying outstanding radiative properties. Briefly, the average emissivity of GTFO in the 3–14 μm band at 1273 K is more than 0.7, which satisfies the design requirements for high emissivity ceramic coatings [28], and dramatically enhances its thermal dissipation of infrared radiation.

It is well known that the high-temperature thermal stability of infrared thermal protective coating materials is an essential factor affecting their protective performance, which is closely related to their practical application life. Therefore, the high-temperature stability of GTFO sample was evaluated with the assistance of a high-temperature test (1773 K, 200 h) in which the test parameters are shown in Fig. S10a, and the sample was subjected to three stages of heating to 1,773 K, holding for 200 h, and natural cooling to room temperature. The XRD results indicate that the phase composition structure of GTFO sample remain the same as before the test throughout the process with no decomposition of the second phase occurs (Fig. 2j). However, the main phase lattice shift behavior increased further, which is possibly related to the elemental diffusion. The dark-field scanning transmission electron microscopy (STEM) image combined with energy dispersive X-ray spectroscopy (STEM-EDS) (Fig. 2l) demonstrates no decomposition of the $GdFeO_3$ particles in the GTFO sample after a long period of high-temperature testing, with a clear interface between the second and main phases, however, its outward elemental diffusion is more serious than that before the high-temperature testing, which is in agreement with the results of the XRD analyses. Additionally, Fig. 2k illustrates the emissivity in the mid-infrared band (MIR, 2.5–14 μm) of the GTFO sample after high-temperature testing. Remarkably, the optical absorption properties of the GTFO samples exhibit a stable trend, with barely changes in its emissivity compared to the previous tests. Its average emissivity at MIR (Fig. S10b) still reaches above 0.9, confirming the excellent thermal stability and infrared radiation performance of the GTFO sample.

2.3. Radiation mechanism behind the GTFO

Definitely, the mechanism of high infrared radiation in GTFO is related to its chemical bonding and electronic structure. Therefore, we probed some regions in GTFO using X-ray photoelectron spectroscopy (XPS), and its spectra (Fig. S11) show the presence of elements such as Gd, Ta, Fe, and O. The Fe 2p spectra (Fig. 3a) exhibited that there appeared two characteristic peaks of 2p orbitals for both Fe^{3+} and Fe^{2+} iron ions, with two main peaks and two satellite peaks, separately. In which, the main peaks at 711.18 eV (Fe $2p_{3/2}$) and 723.52 eV (Fe $2p_{1/2}$) belong to Fe^{3+}, while the main peaks at 709.92 eV (Fe $2p_{3/2}$) and 723.01 eV (Fe $2p_{1/2}$) belong to Fe^{2+}. Additionally, the satellite peaks of Fe^{3+} and Fe^{2+} were at 719.1 eV, 725.84 eV and 713.95 eV, 724.47 eV, respectively. Meanwhile, in order to further confirm the ratio of Fe^{3+} and Fe^{2+}, we calculated and compared the area ratio of Fe^{3+} and Fe^{2+} characteristic peaks, which was 51:184. This valorization of Fe^{3+} and Fe^{2+} can be considered as producing partial Fe^{3+} ionic cavities, which are retained due to the creation of lattice distortions and ionic polarization fields around the iron ions. Such ionic holes and surrounding lattice distortions are referred to as minor polaritons and have a significant effect on the optical properties of $GdFeO_3$ [29].

It is well known that the concentration of oxygen vacancies inside ceramics has a significant effect on their IR radiation properties [30], thus, we compared the O 1s spectra of the second phase region inside GTFO, $GdFeO_3$ ceramic, the main phase region inside GTFO and GTO ceramic, respectively, as shown in Fig.s 3b, c, d, e. In Fig. 3b, the peaks at 529.93 eV, 531.78 eV, and 532.83 eV can be attributed to lattice oxygen (O_L), vacancy oxygen O_V and surface absorbed oxygen (O_A), respectively. Whereas, in Fig. 3d and e, it is feasible to observe the characteristic peaks of lattice oxygen (O_L) and vacancy oxygen (O_V) solely, as follows: the peaks at 529.98 eV, 531.73 eV, and 530.23 eV, 531.93 eV are assigned to lattice oxygen (O_L) and vacancy oxygen (O_V), individually. As shown in Fig. 3f, the oxygen vacancy content of mentioned four regions are compared, while the GTFO main phase region possesses the highest oxygen vacancy content of 68%, which is much higher than that of GTO ceramics (28%), while the GTFO second phase region also contains a higher content of oxygen vacancies (45%). Due to the incorporation of $GdFeO_3$, there is a consequent lattice distortion and detachment of lattice oxygen within the GTFO sample after sintering, resulting in the formation of a higher content of oxygen vacancies, which speculation is further confirmed by AC-TEM characterization.

Further, the main phase region around $GdFeO_3$ of the GTFO sample was investigated with the aid of focused ion beam (FIB) technique (Fig. S12) and spherical aberration-corrected transmission electron microscopy (AC-TEM) at the atomic resolution level to verify the presence of oxygen vacancies [31]. As shown in Fig. 3g and h, the annular bright field (ABF) and inverted contrast images of this region reveal that there are columns of bright and dark oxygen atoms of different intensities around the Ta/Gd atoms. And one of the darker positions is the region where oxygen vacancies exist [31], illustrated by the yellow circle. Meanwhile, the intensity indication diagrams (Fig. 3i and j) were plotted along the straight-line direction in Fig. 3g, indicating the obvious oxygen vacancies shown by red arrows. It visually verifies the previous XPS test results. In addition, the atomic resolution energy dispersive X-ray (EDX) mapping in Fig. 3k displays that the lattice position of each atom within the two phases is extremely well defined, indicating the stability of the internal atomic arrangement, which is the basis for the thermal, optical, mechanical, and thermal stability.

Moreover, the electronic density of states (DOS) of the second phase ($GdFeO_3$) main (Gd_3TaO_7) phases within GTFO were calculated with the assistance of density-functional theory, as shown in Fig. 3l and m. In particular, the second phase possesses a narrow band gap of 0.74 eV, much lower than that of the main phase with 3.65 eV. Due to the high content of oxygen vacancies, the O 1s orbitals become more concentrated near the Fermi energy level, while the 3d orbitals of elemental Fe

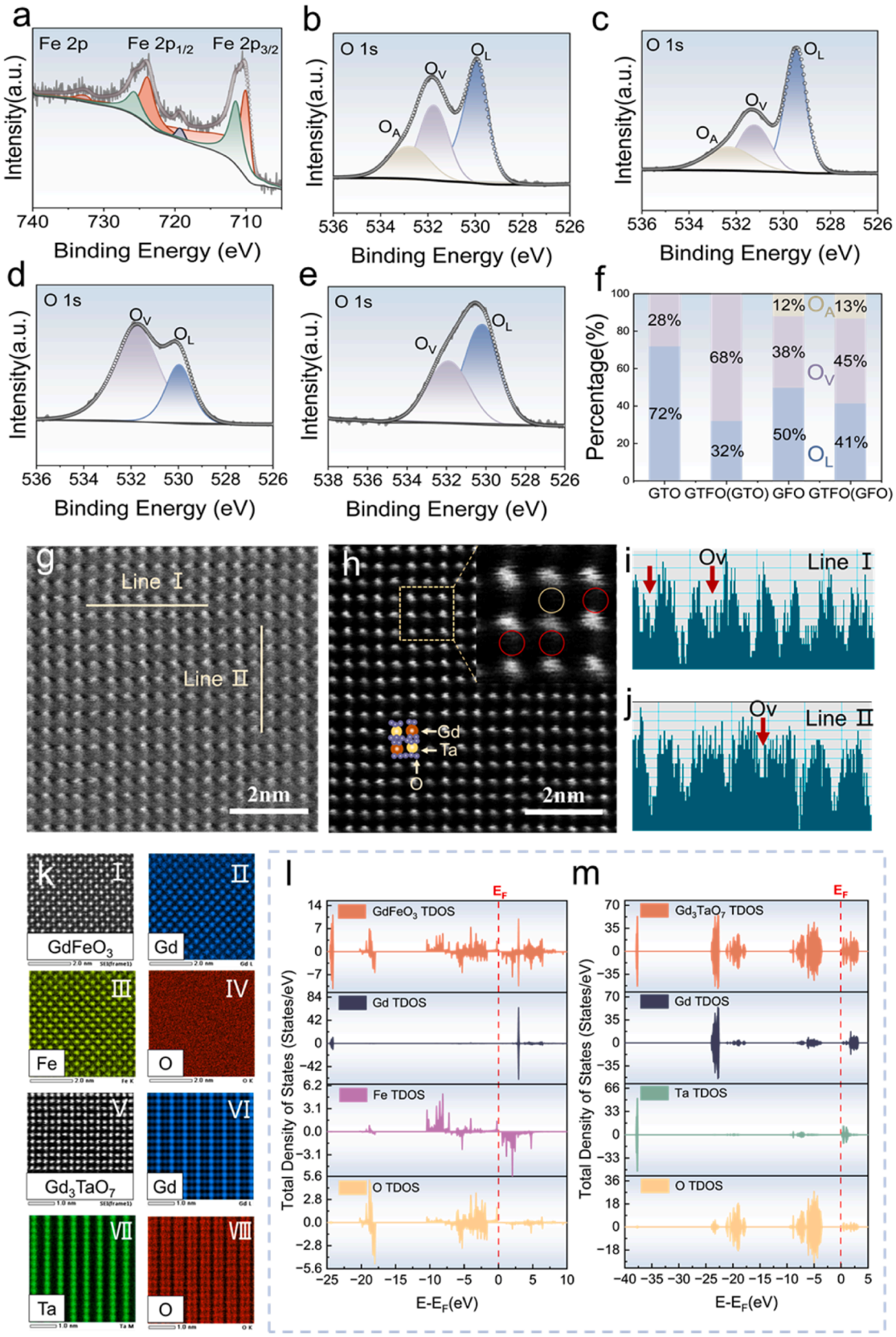

Fig. 3. (a) High-resolution XPS spectra of Fe 2p in GTFO sample; (b–e) High-resolution XPS spectra of O 1s in different sample, including the second phase region inside GTFO sample, $GdFeO_3$ ceramic sample, the main phase region inside GTFO sample, and GTO sample, respectively; (f) Oxygen percentage of O_A, O_V, and O_L; (g). ABF image of GTFO sample viewed along [100] zone axis; (h) Inverted contrast ABF image, where the yellow and red circles represent oxygen and oxygen vacancies, respectively; (i,j) Line contours along the horizontal (i) and vertical (j) directions relative to the markings in (h), where oxygen vacancies are marked with red arrows; (k) Atomic-resolution HAADF-STEM image and corresponding EDX maps for $GdFeO_3$ region and Gd_3TaO_7 region of GTFO sample; (l) TDOS of $GdFeO_3$ and PDOS of all elements in it; (m) TDOS of Gd_3TaO_7 and PDOS of all elements.

have a high density near the Fermi energy level, and there are valence changing behaviors with the partial transformation of Fe^{3+} to Fe^{2+}, which gives origin to the impurity energy level. As a result, the presence of oxygen vacancies, the cationic valuational behavior, and orbital hybridization lead to a narrow bandgap in $GdFeO_3$, which signifies a low energy separation between the valence and conduction bands, assisting more in electron leaps. A massive number of electrons in the valence band are capable of leaping to higher energy levels and conduction bands upon absorption of infrared radiation, which results in high infrared absorption. According to Kirchhoff's law [32], absorption rate=emission rate, i.e., compared with GTO, GTFO has a significant improvement in absorption and emission in the infrared band, which is consistent with the previous results. Based on the mentioned mechanism, it is an excellent design strategy to improve the IR emissivity of rare earth tantalate ceramics by introducing a highly absorbing second phase as well as enhancing the oxygen vacancies and lattice distortions of the material.

2.4. Thermal properties

Fig. 4a exhibits the total thermal diffusivities (D_{total}) of GTFG and GTO. Before 1,273 K, the D_{total} of all the samples decreased with increasing temperature, which can be attributed to the reduction of the phonon mean free range resulting from the phonon Umklapp scattering effect. However, the D_{total} of the GTO sample increases unexpectedly after 1,273 K, probably due to its being semi-translucent in IR wavelength and the increase in the percentage of high-temperature radiative thermal conductivity, which results in an obvious high-temperature thermal radiation effect, and similar phenomena have been reported in the relevant literature [32]. The total thermal conductivities (k_{total}) of GTFG and GTO in Fig. 4b are obtained from Eq. (4), and the variation rule of both with temperature is similar to that of Fig. 4a. Satisfactorily, the k_{total} of GTFO and GTO samples at 1473 K are basically identical (with 1.62 W m^{-1} K^{-1} and 1.61 W m^{-1} K^{-1}, respectively), and the k_{total} curves of GTFO follow a continuous decreasing trend. These results also demonstrate that the $GdFeO_3$ particles barely have a negative effect on the k_{total} of the GTO matrix. For high-temperature semi-transparent oxide ceramics such as 8YSZ, $RE_2Zr_2O_7$, and RE_3TaO_7, e.g., the total thermal conductivity (k_{total}) at elevated temperatures (especially over 1073 K) can be determined by a sum of phonon and photon thermal conductivities [34].

Herein, to further evaluate the radiative thermal conductivities (k_{photon}) of GTFO and GTO, we tested the phonon thermal conductivities (k_{phonon}) of the two samples, as shown in Fig. 4c. For the GTO sample, the k_{phonon} at room temperature is about 1.79W·m^{-1}·K^{-1}, which decreases to 1.35 W m^{-1} K^{-1} at 1473 K, due to phonon-phonon scattering, and oxygen vacancy [33]. At 1473 K, the k_{phonon} of the GTFO sample was observed to be 1.58 W m^{-1} K^{-1}, compared with the GTO sample, possibly due to the introduction of $GdFeO_3$ phase with higher thermal conductivity within GTFO. However, Fig. 4c still confirms the phonon conduction mechanism in GTFO, which is limited by intrinsic phonon scattering, and the phonon thermal conductivity is negatively correlated with temperature. An approximate estimation of the radiative thermal conductivity was attempted from the difference between the k_{total} and the k_{phonon} [34], which is plotted in Fig. 4d. The radiative thermal conductivity (k_{photon}) profiles in Fig. 4d similarly confirm this observation, where the approximate radiative thermal conductivity of GTO rises significantly with temperature and that of GTFO (0.04 W m^{-1} K^{-1}) is inhibited to a much lower level. It indicates that there is significant thermal radiative transmittance in the GTO sample, while the GTFO sample suppresses this thermal radiative transmittance behavior, matching the NIR transmittance test results in Fig. S9. The significant reduction in k_{photon} of this composite can be attributed to a mismatch between the refractive indices of Gd_3TaO_7 (n=1.8) and $GdFeO_3$ (n=2.4) [35,36]. The continuous scattering of photons at the heterogeneous grain boundaries and interfaces of Gd_3TaO_7 and $GdFeO_3$ results in a significant decrease in the k photons of GTFO. Definitely, the excellent thermal radiation shielding performance of the GTFO sample is due to their high absorption coefficient, which hinders the transmission of thermal radiation within itself. In summary, the excellent infrared radiation behavior and low photon thermal conductivity of GTFO material system enable it to improve thermal protection performance by increasing outward heat dissipation and reducing internal heat transfer, as shown in Fig. 4e.

For evaluating TBC candidate materials, the ratio of their elastic modulus to thermal conductivity (E/k) and the product of thermal expansion coefficient to elastic modulus (CTE×E) are a widely used basis of evaluation, with higher E/k and lower CTE×E representing the better stiff, insulative properties and lower internal thermal stresses of the material. In addition, common TBC materials, such as YSZ, rare-earth zirconates, exhibit weak absorption properties in the near-infrared band due to their difficult internal carrier migration and wide band gaps [37], as well as significantly influencing their cooling performance in high-temperature environments. Therefore, it is proposed to evaluate the comprehensive thermal protection performance of TBC candidate materials by coupling the IR emissivity (ε) with E/k and CTE×E, as shown in Fig. 4f. And the modulus of elasticity (E) and thermal expansion coefficient (CTE) of the GTFO sample in this work are listed in Table S2. Obviously, we prepared GTFO thermally protection ceramic material that combines a rather high E/k with IR emissivity close to 1, featuring high heat dissipation, high stiffness, and high insulation, compared with the popular thermal barrier materials (YSZ, RE_2ZrO_7, RE_3NbO_7, RE_3TaO_7, $RE_2Hf_2O_7$) [18,34,38–43]. Based on the mentioned analysis, it can be concluded that the GTFO sample exhibits excellent overall performance in terms of infrared radiation, thermal stability, and thermal conductivity. As a validation, we used an infrared camera to record the difference in surface temperatures of GTFO and GTO samples after propane ablation experiments of different times (Fig. 4g). Therein, the propane flame temperature was close to 1773 K, the environmental temperature was around 253 K, and the ablation times were 10 S, 20 S, and 30 S, respectively. The color difference in the IR images is determined by the emissivity of the samples, and the GTFO sample presents a higher emissivity in the IR band, resulting in a higher surface radiation temperature and a brighter IR image. Notably, the difference in IR radiation capabilities between GTFO and GTO is weakened by the narrower range of bands tested with the IR camera (7–14 μm). Nevertheless, the GTFO sample provides an exciting concentration of excellent thermal emissivity, thermal stability, low thermal conductivity, and outstanding toughness, rendering it a great potential for high-temperature thermal management applications such as aerospace field.

2.5. Mechanical properties and fracture behavior

The mechanical properties (hardness and fracture toughness) of the coating materials are essential for their stability in practical applications. Table S2 also lists the mass density and mechanical properties of the GTO and GTFO samples. The results show that the GTO and GTFO samples have similar mass densities, (8.28±0.21 g/cm^3 and 8.33±0.11 g/cm^3, respectively). Moreover, the GTFO sample exhibits a higher hardness of 14.3±0.28 GPa, while the GTO sample is 10.51 ± 0.56 GPa. Fig. 5a and b demonstrate the representative Vickers indentation morphology of GTO and GTFO samples on polished surfaces. According to the criterion of the indentation method for evaluating the fracture toughness on ceramic surfaces (c < 2.5a, a is half of the diagonal of the indentation, and c is the radius of the crack), combined with the SEM images in Fig. 5a and b, it can be concluded that the fracture toughness K_{IC} computed by the method is highly credible. Fig. 5c exhibits the fracture toughness and Vickers hardness of the GTFO in this study compared with the reported rare earth oxide ceramic materials for thermal barrier coatings [39–42]. Significantly, compared to other TBC ceramics, such as rare-earth zirconates, niobates, and hafnates etc., the

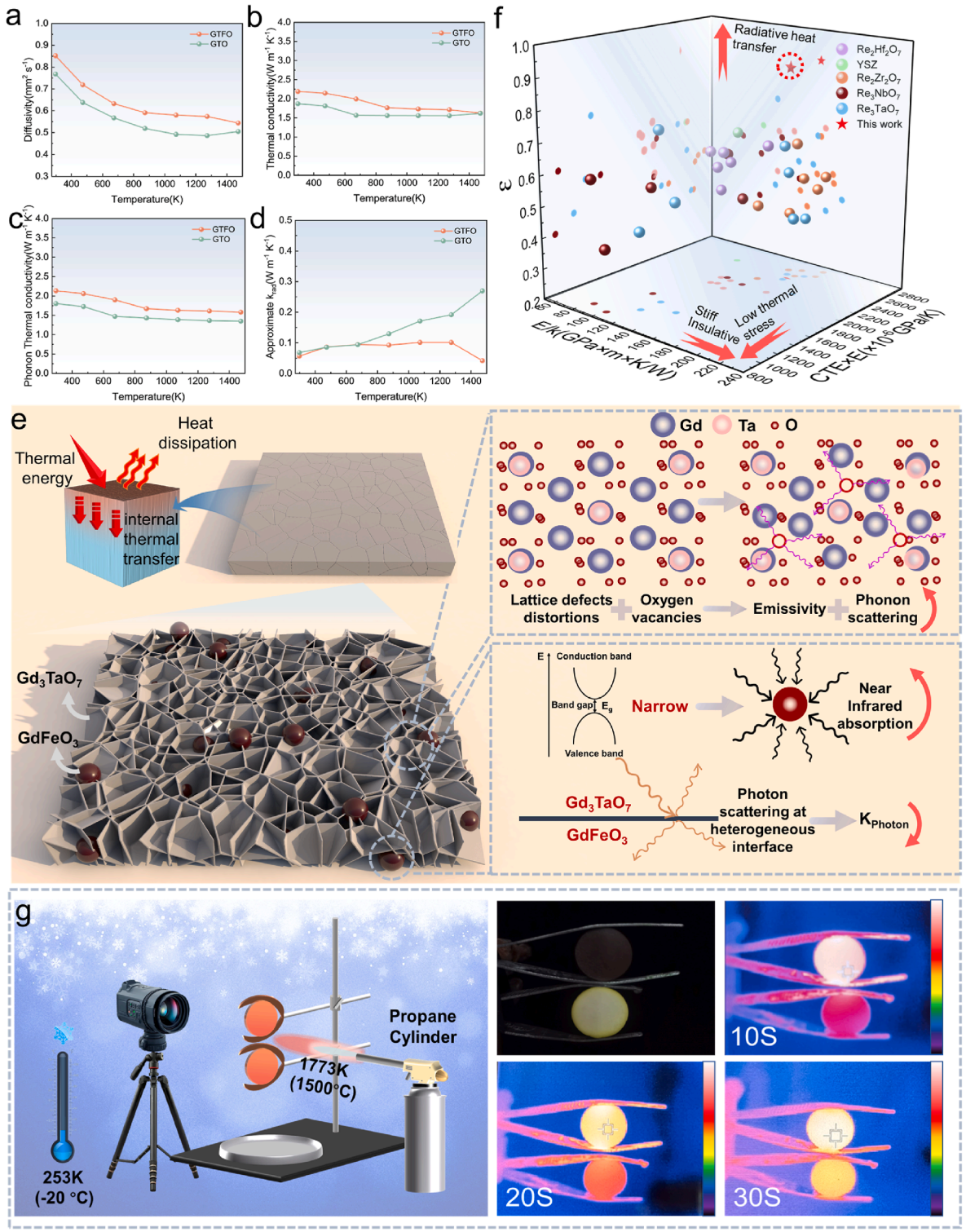

Fig. 4. (a) Thermal diffusivity of GTFO and GTO samples; (b) Total thermal conductivity of GTFO and GTO samples; (c) Phonon thermal conductivity of GTFO and GTO samples; (d) Approximate photon thermal conductivity of GTFO and GTO samples; (e) Mechanism diagram of enhanced thermal protection properties for GTFO materials; (f) the ratio of elastic modulus to thermal conductivity (E/k) and the product of thermal expansion coefficient to elastic modulus (CTE × E) of TBC materials [18,34,38–43]; (g) Infrared photographs of GTFO and GTO samples after different times (10S, 20S, 30S) of propane ablation.

GTFO sample has a surprisingly high toughness (2.3±0.05 MPa $m^{1/2}$), which is similar to that of YSZ. It indicates the enormous application potential of the GTFO material system in the TBCs field. This enhancement of hardness and fracture toughness of GTFO is intimately related to the diffusely distributed $GdFeO_3$, which will be discussed later. Fig. 5d–g illustrates the crack extension behavior of the GTFO samples with a typical crack propagation path through the crystal. Firstly, the cracks are significantly hindered in expanding to the $GdFeO_3$ particles, deflecting, with a large number of cracks winding around the bends and internal energy being absorbed. Secondly, the cracks are bridged in the extension process, and the energy is released through the shedding of spherical $GdFeO_3$ particles as well as friction. In addition, the bifurcation at the

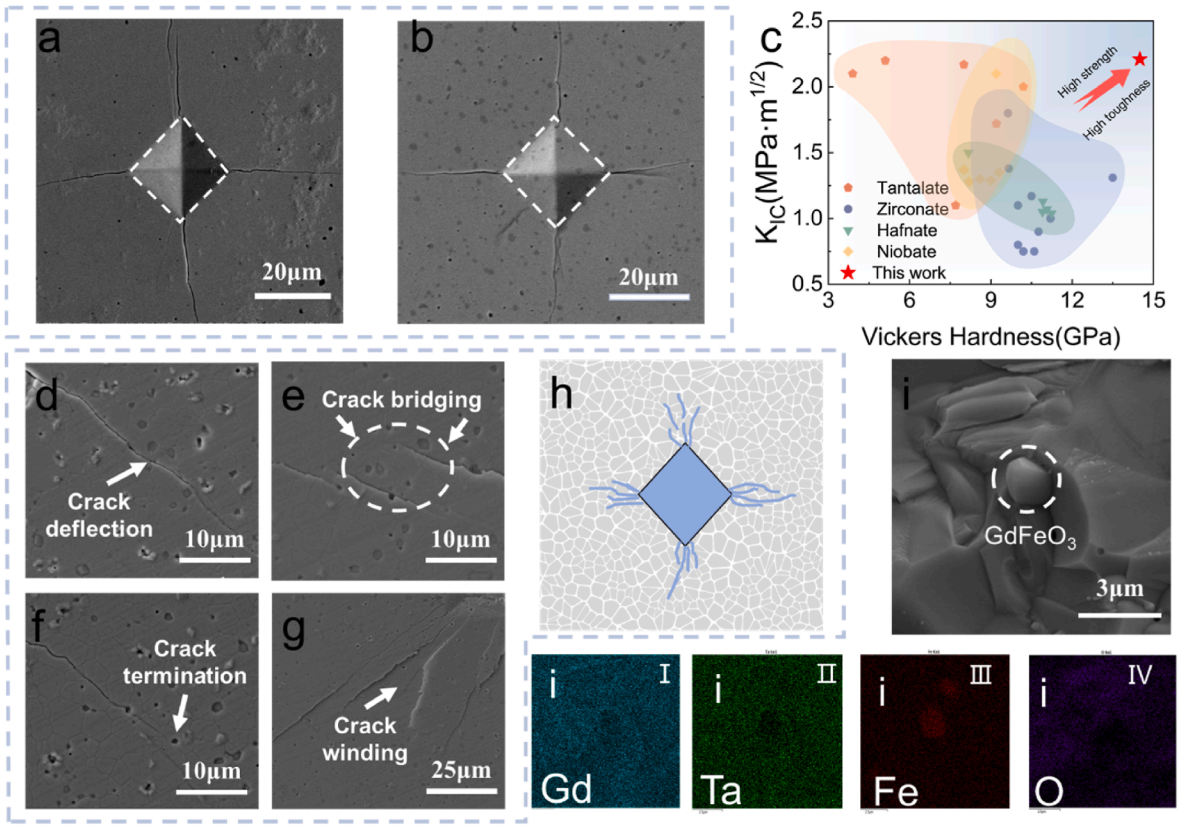

Fig. 5. (a) SEM image of a representative Vickers indentation of the GTO sample with a load of 4.9 N; (b) SEM image of a representative Vickers indentation of the GTFO sample with a load of 4.9 N; (c) Fracture toughness versus Vickers hardness values for the GTFO sample and the previously reported TBC materials [39–42]; (d–g) High magnification SEM images of crack extension behavior in GTFO sample; (h) Crack extension model of GTFO sample; (i) Fracture morphologies and corresponding EDS mapping of GTFO sample.

crack end further consumes energy. Fig. 5h exhibits the crack extension model of GTFO, where the cracks inside the GTFO sample have outstanding toughness due to the large number of deflections, entanglements, bridging, and bifurcations. Fig. 5i shows the fracture morphology of the GTFO sample after bending tests at room temperature, where the fracture characteristics of the sample can be recognized as mixed fracture, containing both extended-crystal fracture and through-crystal fracture. In particular, the intact spherical $GdFeO_3$ particles exposed on the fracture surface can be observed in Fig. 5i. It indicates that the flexural strength of the $GdFeO_3$ particles is superior to that of the Gd_3TaO_7 matrix, so that the $GdFeO_3$ particles inside the GTFO can be considered the mechanically enhanced phase.

3. Conclusion

In summary, a composite rare-earth tantalate ceramic (GTFO) coupled with high emissivity (close to 0.9, 0.78–14 μm), low thermal conductivity (1.62 W m^{-1} K^{-1}~1473 K), and high fracture toughness (2.3 MPa m$^{1/2}$) has been successfully developed. Among them, the spherical second-phase $GdFeO_3$ particles are close to 1.5 μm in size and are diffusely distributed in the Gd_3TaO_7 matrix. The polar absorption mechanism triggered by the variable valence state behavior of Fe^{2+}/Fe^{3+} inside $GdFeO_3$ combined with increased oxygen vacancies (68%) greatly reduces the difficulty of electron absorption, thus leading to the high absorptivity of GTFO in the NIR region (0.78–2.5 μm). Moreover, the lattice distortion and extra lattice vibrations from second-phase doping maintain the emissivity (close to 0.9) at a high level in the mid-infrared band (MIR, 2.5–14 μm). In addition, GTFO maintains a low thermal conductivity (1.62 W m^{-1} K^{-1}) and effectively suppresses the upward curvature of the thermal conductivity curve due to thermal radiation at high temperatures (above 1,273 K), which, in combination with the high emissivity, results in effective thermal insulation. In addition, GTFO has a high fracture toughness due to the effective inhibition of crack propagation by the $GdFeO_3$ particles. Notably, the emissivity of the GTFO remained stable even after a long thermal stability test at high temperatures (1,773 K, 200 h), indicating its excellent thermal stability. This tantalate ceramic is anticipated to provide considerable advantages as an excellent candidate for radiant heat management systems under extreme temperature conditions. Moreover, the tremendous potential of this design strategy in advancing the next generation of TBC materials facilitates its application in various fields, including aerospace.

4. Experimental section

Materials preparation: In this paper, tantalate composite ceramics were synthesized by the secondary calcination and solid phase reaction method. In brief, the dry oxides containing Gd_2O_3 (99.99%, Shanghai Naiou Nano Technology Co., Ltd., China) Ta_2O_5 (99.99%, Ningxia Orient Tantalum Industry Co., Ltd., China) and Fe_2O_3 (analytically pure, Shanghai St-Nano Science & Technology Co., Ltd., China) were weighed according to the stoichiometric ratios of Gd_3TaO_7 and $GdFeO_3$ then ground together with anhydrous ethanol and zirconium oxide beads in a planetary ball mill at 400 rpm for 15 h. The ball-milled slurry was then rotary evaporated and dried in an oven at 393 K for 12 h. Then, the dried powder was ground in an agate mortar and through a 400-mesh sieve. Subsequently, the powders were transferred to an alumina crucible and calcined in an air atmosphere for 6 h until the reaction was complete (purity confirmed by XRD), where the Gd_3TaO_7 and $GdFeO_3$ powders were calcined at 1723 K and 1573 K respectively. The raw powders of

Gd_3TaO_7 and $GdFeO_3$ obtained after calcination were then re-mixed, reground, and weighed according to the molar ratio of 9:1, and the ball milling, drying and sieving were repeated to obtain the mixed powders. Then cold isostatic pressing at 220 MPa was used to produce ceramic green blocks with dimensions of Φ30 mm×2 mm. Finally, the composite phase ceramic samples (identified as GTFO) were prepared by pressure-less sintering at 1823 K for 10 h. In contrast, pure phase Gd_3TaO_7 ceramic samples (identified as GTO) with similar porosity and grain size were produced by the same process with an unpressurised sintering temperature of 1,923 K. To ensure the accuracy of the microstructural and related property data, both ceramic systems were sintered multiple times and more than ten samples of each ceramic were obtained. Afterwards, the samples were processed into Φ12.7 mm×1 mm discs and Φ30 mm×1 mm discs, respectively, to satisfy the test requirements of thermal conductivity and emissivity. All samples were polished with 400 #–3000 # diamond sandpaper for several times before testing.

Characterization technique: The phase structures of the prepared samples were determined by XRD (X' PERT, 40 kV/40 mA, Cu Kα, λ=1.54 Å, PLAN, PAN Analytical, The Netherlands). For the physical phase, the lattice parameters were acquired by Rietveld refinement in the MDI Jade software package. The surface micromorphology and elemental composition of the samples were characterized using a field emission scanning electron microscope (Nanolab 600i, Helios, 20 kV, U.S.A.) and its associated energy dispersive spectrometer (EDS, EDAX Inc., Mahwah, NJ) detector. Electron backscattering diffraction (EBSD) analyse was carry out by using field emission scanning electron microscopy (Gemini-560, Zeiss, Germany).The samples were subjected to polishing and thermal etching (1823 K, 30 min) before SEM characterization. The vibrational frequencies of the samples were determined using Raman spectroscopy (HORIBA Jobin Yvon, LabRAM HR Evolution, HeNe laser at 632.81 nm). Fourier Transform Infrared (FT-IR) spectra of the samples were determined using a Perki Elmer Frontier spectrometer (Nicolet is50, Thermo, USA, resolution 0.02 cm^{-1}) in the spectral range of 400–4000 cm^{-1}. The microstructure was further observed by high-angle annular dark-field scanning translation electron microscope images (HAADF-STEM, FEI Talos F200x, 200 kV), and elemental mapping was also performed using an energy-dispersive X-ray analyzer (EDX) connected with the TEM unit. In addition, oxygen vacancies were characterized using Spherical Aberration Corrected Transmission Electron Microscope (AC-TEM, JEM-ARM 300F, JEOL, Japan). The distribution of nanoscale elements in samples are also investigated by STEM-EDS analysis. Helios 5 UX DualBeam (Thermo Fisher, USA) device was used to prepare samples for AC-TEM characterization by the focused ion beam (FIB) technique (Helios 5 UX DualBeam, Thermo Fisher Scientific, USA). Simultaneously, the oxygen vacancies of the prepared ceramic samples were similarly determined by X-ray photoelectron spectroscopy (XPS, K-Alpha, Thermo Fisher Scientific, USA).

Measurements of spectral, thermal, and mechanical properties: The hemispherical reflectivity and near-infrared (NIR) transmittance of the samples in the 400–2,000 nm and 400–2,500 nm bands were measured by different UV/Vis spectrophotometers (Lambda 750 and Lambda 1050, preferred by PerkinElmer) with an integrating sphere (InGaAs) and $BaSO_4$ as a reference sample. The broad-band spectral radiative emissivity (2.5–14 μm) of the samples at room temperature was measured by a Fourier transform infrared spectrometer (JASCO FT/IR-6100). Whereas, the spectral radiative emissivity (2.5–14 μm) at high temperatures was measured by homemade equipment based on the energy comparison method. The average emissivity ($\bar{\varepsilon}$) for the λ_1–λ_2 bands was calculated by the following equation (4) [44]:

$$\bar{\varepsilon} = \frac{\int_{\lambda_1}^{\lambda_2} \varepsilon(\lambda) \frac{C_1\lambda^{-5}}{e^{\frac{C_2}{\lambda T}}-1} d\lambda}{\int_{\lambda_1}^{\lambda_2} \frac{C_1\lambda^{-5}}{e^{\frac{C_2}{\lambda T}}-1} d\lambda} \quad (4)$$

The thermal diffusivity (D) was measured by the laser thermal conductivity meter (LFA-467, Netzsch, Germany) and corrected to obtain the total thermal diffusion coefficient and the phonon thermal diffusion coefficient by using the Cape-Lehman model [45] and the Mehling radiation model [46], respectively. Differential scanning calorimetry (DSC) analyzer (METTLER-TGA/DSC1, Switzerland) was used to measure the heat capacity Cp. Finally, the thermal conductivity of the fully dense ceramic block was obtained using Kelemen's formula [37]:

$$k = D \cdot Cp \cdot \rho \Big/ \left(1 - \frac{4\varphi}{3}\right) \quad (5)$$

where D is the thermal diffusivity ($mm^2 \cdot S^{-1}$), Cp is the heat capacity ($J \cdot K^{-1} \cdot g^{-1}$), ρ is the density (g/cm^3), φ is the porosity of the sintered specimen.

The thermal expansion properties of the bulk specimens were investigated using a thermal expansion meter (DIL 801, Netzch, Germany).

Hardness values (Hv) were determined using Vickers micro-hardness tester (FUTURE, FM-ARS9000, Japan) by indenting 10 randomly selected points on the surface of the samples with an average force of 4.9 N for 15 s. The modulus of elasticity (E) was determined by a nano-indentation tester (G200, Agilent Technologies, Inc., USA) at a pressure of 500 mg, and each sample was tested more than 10 times at random locations on the surface, and the test results were averaged over all the results to ensure the accuracy of the experimental data. In addition, the fracture toughness of the samples was predicted using Vickers indentation and the Antis equation [47].

$$K_{IC} = 0.016 \left(\frac{E}{H}\right)^{\frac{1}{2}} \frac{P}{c^{\frac{3}{2}}} \quad (6)$$

where H is the Vickers hardness ($(N \cdot mm^{-2})$), P is the applied load of 4.9 N, c is the average crack length (mm), E is the Young's modulus.

First principle calculations: Density Functional Theory (DFT) was employed in the calculations using the generalized gradient approximation correction for solids [48] from the Vienna Ab initio Computational Simulation Package (VASP) [49,50]. In order to better deal with the localization effect of d-orbital electrons in transition group atoms, a Hubbard-like correction (U_{eff}=4 eV for $GdFeO_3$, U_{eff}=6 eV for Gd_3TaO_7) was used [51]. Ion nuclei were treated by the projection-enhanced approximation (PAW) [52,53] with Monkhorst Pack grid k-point mesh of 2 × 2 × 2 ($GdFeO_3$) and 3 × 2 × 3 (Gd_3TaO_7), and the structure optimization started at the point of Hermann-Feynman force up to 0.005 eV/μA, converging to a total energy of 10^{-8} eV. In particular, all calculations were performed with a plane wave energy truncation of 480 eV and unfolded as a plane wave with a truncated PAW. In addition, in the case of elasticity and vibration, an enlarged energy cutoff of 520 eV was utilized to guarantee its convergence.

CRediT authorship contribution statement

Enyu Xie: Writing – review & editing, Writing – original draft, Formal analysis, Data curation, Conceptualization. **Shuqi Wang:** Writing – review & editing, Resources, Funding acquisition. **Guoliang Chen:** Writing – review & editing, Funding acquisition. **Yongchun Zou:** Writing – review & editing, Resources, Data curation. **Jianghong Zhang:** Software. **Yaming Wang:** Writing – review & editing, Resources, Funding acquisition. **Qingyuan Zhao:** Formal analysis, Data curation. **Zijian Peng:** Formal analysis, Data curation. **Junteng Yao:** Validation, Formal analysis, Data curation. **Jiahu Ouyang:** Resources. **Dechang Jia:** Resources. **Yu Zhou:** Writing – review & editing, Resources. **Valentina L. Stolyarova:** Writing – review & editing, Supervision.

Acknowledgements

The partial supports from the NSFC Grant nos. 52301084, U21B2053, and 52301085, Postdoctoral Fellowship Program of CPSF (YJB20240056), Aeronautical Science Foundation (2023M045077001), Open Project Funding of State Key Laboratory for High Performance Tools (GXNGJSKL 2024), Opening Project Fund of Materials Service Safety Assessment Facilities (MSAF-2024-007), and the Fundamental Research Funds for the Central Universities are gratefully acknowledged. Thanks to eceshi (www.eceshi.com) for the Specific Heat Capacity (*Cp*) analysis.

Appendix A. Supplementary data

Supplementary data to this article can be found online at https://doi.org/10.1016/j.apmate.2025.100318.

References

[1] M. He, B. Zhao, X. Yue, Y. Chen, F. Qiu, T. Zhang, Infrared radiative modulating textiles for personal thermal management: principle, design and application, Nano Energy 116 (2023) 108821.
[2] Y. Liu, D. Jiang, M.M. Hessien, M. Mahmoud, M. Xu, Z.M. El-Bahy, Enhanced thermal and mechanical properties of boron-modified phenolic resin composites with multifiller system for aerospace applications, Adv. Compos. Hybrid Mater. 7 (5) (2024) 1–16.
[3] L. Liang, X. Wang, C. Zhang, K. Lu, G. Tan, Y. Dong, Y. Shi, J. Qi, T. Lu, New lead-free chemistry for in-situ monitoring of advanced nuclear power plant, Adv. Powder Mater. 3 (5) (2024) 100229.
[4] J.L. Barton, Electrification of the chemical industry, Science 368 (6496) (2020) 1181–1182.
[5] K.M. Chung, S.R. Adapa, Y. Pei, R.H. Yeerella, L. Chen, S. Shivakumar, W. Huang, Z. Liu, S. Cai, J. Luo, Low thermal conductivity and diffusivity at high temperatures using stable high-entropy spinel oxide nanoparticles, Adv. Mater. 37 (6) (2024) 2406732.
[6] X. Li, H. Luo, D. Zhai, Y. Wan, G. He, D. Hu, H. Hou, D. Zhang, S. Zhang, Enhanced capacitive energy storage of polyetherimide at high temperatures by integration of electrical insulation and thermal conductivity, Adv. Powder Mater. 100286.
[7] S. Zhou, Z. Qiu, M. Strømme, C. Xu, Solar-driven ionic power generation via a film of nanocellulose@ conductive metal–organic framework, Energy Environ. Sci. 14 (2) (2021) 900–905.
[8] X. Wang, Z. Huang, Y. Yao, H. Qiao, G. Zhong, Y. Pei, C. Zheng, D. Kline, Q. Xia, Z. Lin, Continuous 2000 K droplet-to-particle synthesis, mater, Today Off. 35 (2020) 106–114.
[9] Z. Peng, Q. Ma, Y. Cui, S. Chen, F. Cao, X. Xiong, Tailored Csf/$HfC_{0.7}6N_{0.24}$ composites for superior ablation resistance at 3000°C, Adv. Powder Mater. 4 (2) (2025) 100281.
[10] P. Chen, P. Xiao, Z. Li, Y. Wang, X. Tang, Y. Li, Water vapor corrosion behavior and failure mechanism of air sprayed bi-layer $Yb_2Si_2O_7$/SiC and tri-layer $Yb_2Si_2O_7$/(SiC_w-Mullite)/SiC environmental barrier coating, Adv. Powder Mater. 2 (1) (2023) 100064.
[11] S. Li, E. Yang, Y. Li, X. Mo, Z. Chen, Z. Zhou, G. Tao, Y. Long, B. Hu, Self-adaptive energy-efficient windows with enhanced synergistic regulation of broadband infrared thermal radiation, Nano Energy 129 (2024) 110023.
[12] W.M. Wang, B.H. Liu, C.Y. He, P. Zhao, S.J. Zhao, Z.Q. Wang, Z.W. Lu, H.X. Guo, G. Y. Ren, G. Liu, High-entropy engineering for broadband infrared radiation, Adv. Funct. Mater. 33 (43) (2023) 2303197.
[13] F. Ji, Y. Huang, F. Wang, L. Kobera, F. Xie, J. Klarbring, S. Abbrent, J. Brus, C. Yin, S.I. Simak, Near-infrared light-responsive cu-doped $Cs_2AgBiBr_6$, Adv. Funct. Mater. 30 (51) (2020) 2005521.
[14] C.B. Simmons, A.J. Akey, J.P. Mailoa, D. Recht, M.J. Aziz, T. Buonassisi, Enhancing the infrared photoresponse of silicon by controlling the fermi level location within an impurity band, Adv. Funct. Mater. 24 (19) (2014) 2852–2858.
[15] K. Zhang, L. Hao, M. Du, J. Mi, J.N. Wang, J.p. Meng, A review on thermal stability and high temperature induced ageing mechanisms of solar absorber coatings, Renew. Sustain. Energy Rev. 67 (2017) 1282–1299.
[16] Y. Li, M. Chen, B. Liu, Y. Zhang, X. Liang, X. Xia, Heteroatom doping: an effective way to boost sodium ion storage, Adv. Energy Mater. 10 (27) (2020) 2000927.
[17] Z. Yang, M. Huang, R. Yang, J. Sun, X. Zhang, W. Pan, C. Wan, Near-infrared trapping by surface plasmons in randomized platinum-ceramic metamaterial for thermal barrier coatings, Small Methods 7 (6) (2023) 2201691.
[18] M. Huang, J. Liang, P. Zhang, Y. Li, Y. Han, Z. Yang, W. Pan, C. Wan, Opaque $Gd_2Zr_2O_7$/$GdMnO_3$ thermal barrier materials for thermal radiation shielding: the effect of polaron excitation, J. Mater. Sci. Technol. 100 (2022) 67–74.
[19] T. Li, Z. Ma, L. Liu, S. Zhu, Thermal properties of $Sm_2Zr_2O_7$-$NiCr_2O_4$ composites, Ceram. Int. 40 (7) (2014) 11423–11426.
[20] L. Chen, M. Hu, J. Wang, B. Li, J. Feng, Dominant mechanisms of thermo-mechanical properties of weberite-type RE_3TaO_7 (RE=La, Pr, Nd, Eu, Gd, dy) tantalates toward multifunctional thermal/environmental barrier coating applications, Acta Mater. 270 (2024) 119857.
[21] L. Chen, B. Li, J. Feng, Rare-earth tantalates for next-generation thermal barrier coatings, Prog. Mater. Sci. 144 (2024) 101265.
[22] N. Ma, Z. Zhang, P. Nan, W. Bai, K. Li, J. Zhao, S. Zhou, B. Ge, J. Yang, C. Xiao, Phonon symphony of stacked multilayers and weak bonds lowers lattice thermal conductivity, Adv. Mater. 34 (30) (2022) 2202677.
[23] P.S. Chang, B.H. Chen, Y.C. Lin, W.T. Dai, G. Kumar, Y.G. Lin, M.H. Huang, Growth of size-tunable Ag_2O polyhedra and revelation of their bulk and surface lattices, Small 20 (40) (2024) 2401558.
[24] J. Yang, X. Qian, W. Pan, R. Yang, Z. Li, Y. Han, M. Zhao, M. Huang, C. Wan, Diffused lattice vibration and ultralow thermal conductivity in the binary ln–nb–o oxide system, Adv. Mater. 31 (24) (2019) 1808222.
[25] S. Tang, S. Nishimoto, K. Hagihara, M. Yamasaki, Effects of heterogeneous microstructure evolution on the tensile and fracture toughness properties of extruded AZ31B alloys, J. Magnesium Alloys 12 (10) (2024) 4126–4139.
[26] J.R. Nolen, A.C. Overvig, M. Cotrufo, A. Alù, Local control of polarization and geometric phase in thermal metasurfaces, Nat. Nanotechnol. 19 (2024) 1627–1634.
[27] H.G. Hecht, The interpretation of diffuse reflectance spectra, J. Res. Natl. Bur. Stan. A Phys. Chem. 80 (4) (1976), 567-538.
[28] D. Van Wie, D. Drewry, D. King, C. Hudson, The hypersonic environment: required operating conditions and design challenges, J. Mater. Sci. 39 (2004) 5915–5924.
[29] L.M. Carneiro, S.K. Cushing, C. Liu, Y. Su, P. Yang, A.P. Alivisatos, S.R. Leone, Excitation-wavelength-dependent small polaron trapping of photoexcited carriers in α-Fe_2O_3, Nat. Mater. 16 (8) (2017) 819–825.
[30] H. Jin, L. Wang, D.J. Searles, C. Sun, Comparison of the effect of hydrogen incorporation and oxygen vacancies on the properties of anatase TiO_2: electronics, optical absorption, and interaction with water, Sci. Bull. 59 (2014) 2175–2180.
[31] J. Wang, Q. Jin, P. Wu, Z. Zhao, Z. Ge, X. Chong, J. Feng, Unveiling the mechanisms of ultra-low thermal and oxygen-ion conductivity in entropy-stabilized ferroelastic rare-earth tantalates, Acta Mater. 283 (2025) 120523.
[32] S. Yang, M. Liu, C. Zhao, S. Fan, C.W. Qiu, Nonreciprocal thermal photonics, Nat. Photonics 18 (2024) 412–424.
[33] S. Shin, Q. Wang, J. Luo, R. Chen, Advanced materials for high-temperature thermal transport, Adv. Funct. Mater. 30 (8) (2020) 1904815.
[34] H.S. Aziz, C. Wan, Y. Xing, M. Sajid, M. Shahid, W. Pan, Low radiative heat transfer realized by 8YSZ/$LaAl_{11}O_{18}$ composites for high-temperature applications, J. Mater. Sci. 57 (40) (2022) 18754–18769.
[35] X.H. Zhu, X.B. Xiao, X.R. Chen, B.G. Liu, Electronic structure, magnetism and optical properties of orthorhombic $GdFeO_3$ from first principles, RSC Adv. 7 (7) (2017) 4054–4061.
[36] E. Xie, G. Chen, S. Wang, Y. Zou, J. Zhang, Y. Wang, Q. Zhao, J. Wang, J. Ouyang, D. Jia, Thermal shielding Gd_3TaO_7-Based thermal barrier ceramic with ultralow NIR transmittance, Small https://doi.org/10.1002/smll.202404567.
[37] G. Chen, H. Fu, Y. Zou, S. Wang, Y. Gao, T. Yue, J. Cao, Y. Wang, J. Qiu, J. Zhao, A promising radiation thermal protection coating based on lamellar porous Ca–Cr co-doped Y_3NbO_7 ceramic, Adv. Funct. Mater. 33 (47) (2023) 2305650.
[38] J. Yang, C. Wan, M. Zhao, M. Shahid, W. Pan, Effective blocking of radiative thermal conductivity in $La_2Zr_2O_7$/$LaPO_4$ composites for high temperature thermal insulation applications, J. Eur. Ceram. Soc. 36 (15) (2016) 3809–3814.
[39] J. Zhu, X. Meng, J. Xu, P. Zhang, Z. Lou, M.J. Reece, F. Gao, Ultra-low thermal conductivity and enhanced mechanical properties of high-entropy rare Earth niobates (RE_3NbO_7, RE= Dy, Y, Ho, Er, yb), J. Eur. Ceram. Soc. 41 (1) (2021) 1052–1057.
[40] L. Cong, S. Gu, W. Li, Thermophysical properties of a novel high entropy hafnate ceramic, J. Mater. Sci. Technol. 85 (2021) 152–157.
[41] R. Liu, W. Liang, Q. Miao, H. Zhao, S. Ramakrishna, B. Ramasubramanian, X. Zhang, Y. Song, X. Gao, J. Du, A novel defect fluorite type high-entropy $(Dy_{0.2}Ho_{0.2}Er_{0.2}Tm_{0.2}Lu_{0.2})_2Hf_2O_7$ ceramic with low thermal conductivity and CTE: a mechanism study, J. Mater. Res. Technol. 27 (2023) 1365–1380.
[42] F.A. López-Cota, N.M. Cepeda-Sánchez, J.A. Díaz-Guillén, O.J. Dura, M.A. López de la Torre, M. Maczka, M. Ptak, A.F. Fuentes, Electrical and thermophysical properties of mechanochemically obtained lanthanide hafnates, J. Am. Ceram. Soc. 100 (5) (2017) 1994–2004.
[43] Q. Zhao, S. Wang, G. Chen, Y. Sun, Y. Zou, E. Xie, Z. Peng, J. Yao, O. Jiahu, Y. Wang, La2Hf2O7 based TBC materials with near-infrared ultra-low transmittance for thermal radiation shielding, Adv. Opt. Mater. https://doi.org/10.1002/adom.202401768.
[44] Z.L. Xi, X. Aday, M. Dong, B.H. Liu, C.Y. He, G.Y. Ren, X.H. Gao, Enhanced broadband infrared radiation from rare Earth orthochromites for high-temperature radiative heat transfer, Chem. Eng. J. 497 (2024) 154905.
[45] J. Cape, G. Lehman, Temperature and finite pulse-time effects in the flash method for measuring thermal diffusivity, J. Appl. Phys. 34 (7) (1963) 1909–1913.
[46] H. Mehling, G. Hautzinger, O. Nilsson, J. Fricke, R. Hofmann, O. Hahn, Thermal diffusivity of semitransparent materials determined by the laser-flash method applying a new analytical model, Int. J. Thermophys. 19 (3) (1998) 941–949.
[47] J. Hu, Q. Yang, S. Zhu, Y. Zhang, D. Yan, K. Gan, Z. Li, Superhard bulk high-entropy carbides with enhanced toughness via metastable in-situ particles, Nat. Commun. 14 (1) (2023) 5717.
[48] J.P. Perdew, A. Ruzsinszky, G.I. Csonka, O.A. Vydrov, G.E. Scuseria, L.A. Constantin, X.L. Zhou, K. Burke, Restoring the density-gradient expansion for exchange in solids and surfaces, Phys. Rev. Lett. https://doi.org/10.1103/PhysRevLett.100.136406.
[49] G. Kresse, J. Furthmüller, Efficient iterative schemes for ab initio total-energy calculations using a plane-wave basis set, Phys. Rev. B 54 (16) (1996) 11169.
[50] G. Kresse, D. Joubert, From ultrasoft pseudopotentials to the projector augmented-wave method, Phys. Rev. B https://doi.org/10.1103/PhysRevB.59.1758.

[51] S.L. Dudarev, G.A. Botton, S.Y. Savrasov, C. Humphreys, A.P. Sutton, Electron-energy-loss spectra and the structural stability of nickel oxide: an LSDA+ U study, Phys. Rev. B https://doi.org/10.1103/PhysRevB.57.1505.
[52] P.E. Blöchl, Projector augmented-wave method, Phys. Rev. B 50 (24) (1994) 17953.
[53] P.E. Blöchl, C.J. Först, J. Schimpl, Projector augmented wave method: ab initio molecular dynamics with full wave functions, Bull. Mater. Sci. 26 (1) (2003) 33–41.

Enyu Xie is now pursuing his Ph.D. degree in Materials Science and Engineering from the Harbin Institute of Technology. His work focuses on advanced high temperature protective powder and ceramic materials with high emissivity and thermal radiation shielding.

Shuqi Wang received his PhD degree in Materials Science and Engineering from the Harbin Institute of Technology. He is particularly interested in researching thermal protective ceramic coating and advanced ceramic materials. He has completed joint research at the Institute of Surface Science, Helmholtz-Zentrum Hereon. He is currently an assistant professor at School of Materials Science and Engineering, Harbin Institute of Technology.

Guoliang Chen received his PhD degree in Materials Science and Engineering from the Harbin Institute of Technology. He is particularly interested in adiation thermophysical simulation and advanced ceramic material development. He has completed joint research at the Nanyang University of Technology. He is currently an assistant professor at School of Energy Science and Engineering, Harbin Institute of Technology.

Yaming Wang received PhD degree in Materials Science and Engineering from the Harbin Institute of Technology. He is Professor of at School of Materials Science and Engineering, Harbin Institute of Technology. He has published more than 160 papers that have been included by SCI, cited more than 6000 times with an h-index of 45, of which two highly cited papers were included in the top 1% of ESI. He is Fellow of the Chinese Society of Mechanical Engineering, Chinese Society for Materials Research, International Society of Bionics, and Surface Engineering Branch of China Mechanical Engineering Society.